Charge density wave modulation and gap measurements in CeTe_{3}

U. Ralević, N. Lazarević, A. Baum, H.-M. Eiter, R. Hackl, P. Giraldo-Gallo, I. R. Fisher, C. Petrovic, R. Gajić, and Z. V. Popović

Phys. Rev. B **94**, 165132 — Published 14 October 2016

DOI: 10.1103/PhysRevB.94.165132

Charge density wave modulation and gap measurements in $CeTe_3$

U. Ralević,[1,2] N. Lazarević,[1] A. Baum,[3] H.-M. Eiter,[3] R. Hackl,[3] P. Giraldo-Gallo,[4] I. R. Fisher,[4] C. Petrovic,[5] R. Gajić,[1] and Z. V. Popović[1]

[1] *Center for Solid State Physics and New Materials, Institute of Physics, University of Belgrade, Pregrevica 118, 11080 Belgrade, Serbia*
[2] *Faculty of Electrical Engineering, University of Belgrade, Bulevar Kralja Aleksandra 73b, 11120 Belgrade, Serbia*
[3] *Walther Meissner Institut, Bayerische Akademie der Wissenschaften, 85748 Garching, Germany*
[4] *Physics and Applied Physics, Stanford University, Stanford, California 94305, USA*
[5] *Condensed Matter Physics and Materials Science Department, Brookhaven National Laboratory, Upton, New York 11973, USA*

(Dated: September 8, 2016)

We present a study of charge density wave (CDW) ordering in $CeTe_3$ at room temperature using a scanning tunneling microscope and Raman spectroscopy. Two characteristic CDW ordering wavevectors obtained from the Fourier analysis are assessed to be $|\mathbf{c}^* - \mathbf{q}| = 4.19\,\mathrm{nm}^{-1}$ and $|\mathbf{q}| = 10.26\,\mathrm{nm}^{-1}$ where $|\mathbf{c}^*| = 2\pi/c$ is the reciprocal lattice vector. The scanning tunneling spectroscopy measurements, along with inelastic light (Raman) scattering measurements, show a CDW gap $\Delta_{\max}$ of approximately 0.37 eV. In addition to the CDW modulation, we observe an organization of the Te sheet atoms in an array of alternating V- and N- groups along the CDW modulation, as predicted in the literature.

PACS numbers: 71.45.Lr, 61.44.Fw, 68.37.Ef, 78.30.-j

I. INTRODUCTION

Charge density waves (CDW) have been a subject of considerable interest in condensed matter physics for many decades.[1] Originally expected and observed in one-dimensional (1D) systems, CDW formation was found also in many 2D materials where the ordered state remains metallic in most of the cases. Occasionally, the CDW phase is in close proximity to other phases such as superconductivity.[2,3]

The rare-earth tritellurides[4] $R\mathrm{Te}_3$ are excellent model systems for systematic studies of the underlying physics for the wide range of tunable parameters such as transition temperature T_{CDW}, Fermi surface shape, c-axis coupling, anisotropic or weak versus strong electron-phonon coupling.[5–12] These compounds have an orthorhombic crystal structure ($Cmcm$ space group) commonly thought of as being 'weakly' orthorhombic, i.e. tetragonal with a 2-fold reduced symmetry due the very subtle difference of the in-plane crystal axes.[5] For the layered quasi two-dimensional (2D) material with the reduced tetragonal symmetry, the CDW ground state can either be bidirectional (checkerboard) or unidirectional (stripes).[5] High resolution x-ray diffraction,[9–11] angle resolved photoemission spectroscopy (ARPES)[13–15] and femtosecond pump-probe spectroscopy[16] showed that lighter rare-earth tritellurides (i.e. $R = \mathrm{La}\ldots\mathrm{Tb}$) host an unidirectional incommensurate CDW well above room temperature. For the heavy rare-earth tritellurides (i.e. $R = \mathrm{Dy}\ldots\mathrm{Tm}$) the upper transition temperature T_{CDW1} is below room temperature, and another transition having an orthogonal ordering vector occurs at $T_{\mathrm{CDW2}} < T_{\mathrm{CDW1}}$.

Scanning tunneling microscopy (STM) studies of $R\mathrm{Te}_3$, performed at low temperatures,[17,18] show that the CDW modulations within the Te square lattice are incommensurate for the lighter $R\mathrm{Te}_3$ compounds. In addition, using STM on $TbTe_3$, Fang *et al.*[17] demonstrated a possible dimerization of the atoms in the Te plane. Slight modification of the atomic arrangement is not unexpected for systems exhibiting charge density waves. In fact, it was already theoretically predicted that the atoms in a square lattice have tendency toward different distortion phases.[19] For $CeTe_3$ electron diffraction experiments suggest structural distortions in the Te sheets, recognised as N and V shaped groups of Te atoms, representing another broken symmetry of the crystal lattice.[9,20] This phenomenon was further studied by Kim *et al.*[21] applying an atomic pair distribution function (PDF) analysis of the x-ray data. The distance between nearest neighbour Te-Te atoms therein was found to have a bimodal distribution indicating the presence of the aforementioned structural distortions. The occurrence of the N and V patterns in the Te sheets is, however, inconsistent with the present STM data, and it is, therefore, an open issue. Moreover, there is a discrepancy between the gap values derived from ARPES[22] and a recent tunnelling study.[18]

In this article, we reveal the CDW modulation in $CeTe_3$ at room temperature and demonstrate the periodic pattern of Te sheet atoms grouped in N and V shapes. We assess the maximal CDW gap $\Delta_{\max}$ by both scanning tunneling spectroscopy (STS) and Raman scattering measurements and find it to be close 0.37 eV.

II. EXPERIMENTAL

Single crystals of $CeTe_3$ were grown by slow cooling of a binary melt. The details are published elsewhere.[6] The samples for STM measurements were prepared at Brookhaven National Laboratory, whereas those for Raman scattering at Stanford University. Because the compound oxidizes in ambient air, the crystals were cleaved with adhesive tape in order to remove the oxidized layer.

The STM measurements were done in ultra-high vacuum at room temperature, using a commercial OMICRON UHV STM system. Topography imaging was done in constant current mode with the bias voltages in range of 0.1-0.9 V applied to the tip. Tilting error compensation, Fourier noise filtering, and scanner distortions removal were done using Gwyydion image processing program.[23] Every STM topograph and its corresponding current image are displayed with their raw Fourier transform, used for the filtering procedure. It should be noted that displayed raw Fourier images have vertical bands of intensities which originate from a large number of noise induced periodic components in the real space images along the fast scanning axis (x axis). These bands are, therefore, measurement artifacts rather than physical features of the sample. STS measurements were done in point probe mode at different locations on the sample surface, also at room temperature. The I-V curves were made for bias voltages ranging from -0.5 V to 0.5 V, with a resolution of 0.02 V, which is comparable to the thermal noise of about 0.026 eV. Consequently, the CDW gap is evaluated with accuracy of $\sim \pm 2 \times 0.026$ eV.

For the Raman scattering experiments we have used the line at 458 nm of an Ar ion laser as an excitation source. The absorbed laser power ranged from 1 to 2 mW to keep the local heating below 5 K in the $50 \times 100\,\mu m^2$-sized focus, as estimated from comparing energy gain and loss spectra.[24] Since there is no phase transition in close proximity a temperature gradient in the spot can be neglected here. The spectra were measured with a resolution of 2.5 cm^{-1} at low energy and 20 cm^{-1} at high energy. The Raman response $R\chi''(\Omega)$ is then obtained by dividing the measured spectra by the thermal Bose factor. We present symmetry-resolved spectra, obtained from linear combinations of spectra measured at the main polarization configurations,[25] in order to separate out the A_{2g} contribution which, in the non-resonant case, is insensitive to the carrier (particle-hole) excitations we are interested in.

III. RESULTS AND DISCUSSIONS

A. STM topography measurements

$CeTe_3$ crystals are layered quasi-2D materials with orthorhombic crystal structure that adopts the $Cmcm$ space group symmetry.[26] The layers are composed of a corrugated CeTe slab sandwiched between two planar Te sheets and connected together via weak van der Waals forces. Figure 1 (a) shows the crystal structure of $CeTe_3$ with the unit cell indicated by dashed lines. For the $Cmcm$ space group the a and c are the in-plane crystal axes and b is the long crystal axis.

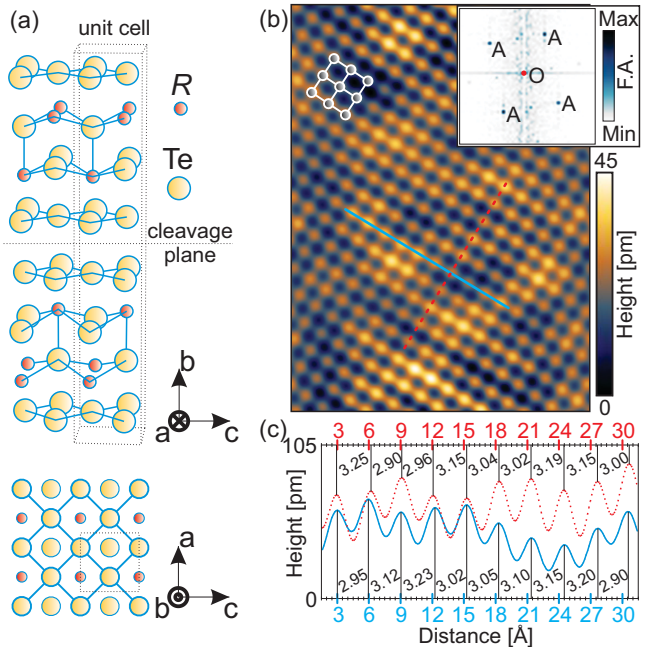

FIG. 1. (Color online) (a) Crystal structure of $CeTe_3$. The lower part shows a view on the top Te layer connected by blue lines oriented at 45° with respect to the a and c axes. The atoms of the R-Te layer are not connected. (b) Filtered STM topograph obtained for V_b =0.8 V and I_s =0.6 nA. The inset shows corresponding Fourier transform (F.A. stands for Fourier Amplitude); (c) Profiles along the solid (blue) and dashed (red) lines in panel (b) showing variation of the Te-Te distances in the Te sheets. The assessed distances between the adjacent Te atoms are written in-between the black vertical lines which show the position of the profiles maxima.

An isolated planar Te sheet with a nearly perfect square lattice has one Te atom in the corresponding unit cell, as opposed to the full crystal which has two distinct Te sites in the planar Te sheets (see the lower part of Fig. 1 (a)), and twelve Te atoms per unit cell (see the upper part of Fig. 1 (a)). As an example, in Fig. 1 (b) the Te square lattice of $CeTe_3$ obtained by setting the bias voltage, V_b, to 0.8 V and the set-point current, I_s, to 0.6 nA, is shown. The corresponding raw Fourier transform is given in the inset. Four distinct peaks, labeled as A, form the reciprocal lattice of the atoms in the Te sheets, and are approximately $2\pi/a_0$=20.43 nm^{-1} from the origin, denoted as O. The average distance between the neighbouring Te atoms can be straightforwardly assessed from the position of the A peaks, i.e. $a_0 = 2\pi/20.43\,nm^{-1}$=0.3075 nm. However, profiles taken along the solid (blue) and dashed (red) lines in Fig. 1 (b) reveal that the distances between the maxima, representing the Te atoms, vary around a constant separation of

$2\pi/20.43\,\mathrm{nm}^{-1}$=0.3075 nm. We find that all of the images, obtained with the same set of tunneling parameters as the one in Fig. 1(b), show similar variation of the Te-Te distances. The variation of the Te-Te distances is very subtle and can not be assessed from the full width at half maximum of the A peaks (see the inset in Fig. 1 (b)). Therefore, the Fourier transform provides the average interatomic distances indicating an ideal Te square lattice, whereas the analysis of the real space images yields irregular Te-Te distances.

Given the weak hybridization between the CeTe slab and the Te sheets,[5,27] the electronic properties of $R\mathrm{Te}_3$ are predominantly determined by the planar Te sheets. Having a weak interaction along the b axis, these compounds are often considered quasi two-dimensional (2D) systems. The main contribution to the CDW comes from the states close to the Fermi level. These states mainly derive from in-plane p_x and p_z orbitals with 5/8 filling due to the underlying CeTe layer, which donates an electron shared between two atoms in the upper and lower Te sheet. The out-of-plane p_y orbital is lower in energy than the in-plane p_x and p_z orbitals and is pushed below the Fermi level. Now, assuming an isolated Te sheet with an ideal square lattice, while neglecting the hopping between p_x and p_z orbitals, one could calculate the Fermi surface[5,12,28] within the corresponding Brillouin zone similar to the one sketched in the inset of Fig. 2 (a) with solid and dashed (red) lines. In the scope of this approximation, there are two possibilities for the nesting vectors, $\mathbf{q}$ and $\mathbf{q}^*$[5,29] (see the inset of Fig. 2 (a)) which are not related by the C_4 symmetry of the assumed host lattice. The rest of the nesting vectors which are symmetry related to the $\mathbf{q}$ and $\mathbf{q}^*$ are described in Ref. 5. The $\mathbf{q}$ vector nests both the p_x (dashed red lines) and the p_z (solid red lines) portions of the Fermi surface, whereas the $\mathbf{q}^*$ nests only the p_x portion of the Fermi surface.[5] Assumption of a purely nesting-driven instability allows the system to choose between the two nesting vectors depending on the strength of the electron-phonon coupling: $\mathbf{q}$ and the stripe symmetry of the CDW state are favored when the coupling is strong.[5] It was recently shown,[12] however, that the inclusion of the interaction between p_x and p_z modifies the Fermi surface, thus, enabling large electron-phonon coupling near the band degeneracy points and renormalization of the phonon frequency only at the $\mathbf{q}$, rather than at $\mathbf{q}^*$. In fact, renormalization at $\mathbf{q}^*$ and the related checkerboard symmetry of the CDW state were not observed experimentally.

Fig. 2 (a) shows the topography of CeTe_3 with clearly visible CDW modulation. This image is obtained for V_b=0.2 V and I_s=0.6 nA. The corresponding Fourier image is given in Fig. 2 (b). As before, there are four peaks representing the Te sheet atoms. They are labeled by A. Peaks labeled by A′ correspond to the additional periodicity arising from the inequality of $\mathbf{a}$ and $\mathbf{c}$ lattice vectors which is a consequence of the orthorhombic crystal structure. In other words, these peaks should exist for any set of tunneling parameters for which the tunneling between the tip and the Te planes is possible. In fact, the A′ peaks exist in Fig. 1 (b) as well, but are barely visible since the inequality between $\mathbf{a}$ and $\mathbf{c}$ is very subtle. The intensity of the A′ peaks in Fig. 2 (b) is "enhanced" by the additional periodicity of the underlaying Ce atoms, whose f states have significant contribution to the tunneling current[18] when the tip is close to the surface, i.e. for lower bias voltages. Accordingly, we assign $\mathbf{c}^*$ and $\mathbf{a}^*$ wavevectors to the A′ peaks, where $|\mathbf{c}^*| = 2\pi/|\mathbf{c}|$ and $|\mathbf{a}^*| = 2\pi/|\mathbf{a}|$. The $\mathbf{c}^*$ connects the origin O and the A′ peak on the main diagonal, and the $\mathbf{a}^*$ is perpendicular to $\mathbf{c}^*$. We assess the magnitude of the two wavevectors to be around $14.4\,\mathrm{nm}^{-1}$.

Apart from A and A′ peaks, the Fourier amplitude image in Fig. 2 (b) exhibits new features in comparison to the one shown in Fig. 1 (b). The peak located below the A′ peak on the main diagonal, Q, corresponds to the $\mathbf{q}$ nesting vector, while the Q′ peak corresponds to the $\mathbf{q}'$ vector. Following the work in Ref. 12 we set the $\mathbf{q}$ as the dominant CDW ordering vector, which further gives $\mathbf{q}' = \mathbf{c}^* - \mathbf{q}$. The magnitudes of $\mathbf{q}$ and $\mathbf{c}^* - \mathbf{q}$ vectors are $10.26\,\mathrm{nm}^{-1}$ and $4.19\,\mathrm{nm}^{-1}$, respectively. The related wavelengths are ∼0.61 nm (distance between (black) circles in Figs. 2 (c) and (d)) and ∼1.5 nm (distance between (red) squares in Figs. 2(c) and (d)), respectively. Displayed in Fig. 2 (e) are the profiles along main and side diagonal of the Fourier image, showing the exact position of the mentioned peaks. The Q peak is more intensive than the Q′ peak which is barely visible on the main diagonal, but clearly visible on the side diagonal. The absence of the Q or Q′ peaks on the main diagonal in Fig. 1 (b), is due to the small, practically negligible, overlapping of the CDW wavefunction, which decays exponentially out of Te sheet, and the tip wavefunction. In fact, significantly reduced overlapping between the two wavefunctions for $V_b = 0.8$ V results in a reduced CDW current signal comparable to the noise level.

In addition to Q and Q′, another peak, which we label as 2Q′, exists on the main diagonal of the Fourier image in Fig. 2 (b). It is located at $8.38\,\mathrm{nm}^{-1}$ from the origin, which is exactly twice the distance between the origin and the Q′ peak. The wave vector connected to this peak is, thus, exactly two times larger than the $\mathbf{c}^* - \mathbf{q}$. Both Q′ and 2Q′ are, in fact, due to the wavevector mixing effect which occurs between the $\mathbf{q}$ and $\mathbf{c}^*$.[17] However, the full mixing effect is not entirely visible in Fig. 2 (b) because the exerted noise masks the rest of the prominent mixing peaks. In Fig. 3 (a), which has been obtained by averaging 34 consecutive Fourier images, this effect becomes more clear. As it can be seen, additional peaks arise by improving the signal-to-noise ratio, both on the main and the side diagonal. Numbers 2 and 6 in Fig. 3 (a) denote two new peaks on the main diagonal specified by $2\mathbf{q} - \mathbf{c}^*$ and $2\mathbf{c}^* - \mathbf{q}$ vectors, respectively. The side diagonal has four peaks corroborating the afore mentioned effect. Their wavevectors, $\mathbf{a}^* + \mathbf{c}^* - \mathbf{q}$, $\mathbf{a}^* + 2\mathbf{q} - \mathbf{c}^*$, $\mathbf{a}^* + 2\mathbf{c}^* - 2\mathbf{q}$ and $\mathbf{a}^* + \mathbf{q}$ are shown by arrows in Fig. 3 (a). Finally, Fig. 3 (b) displays line cuts along the

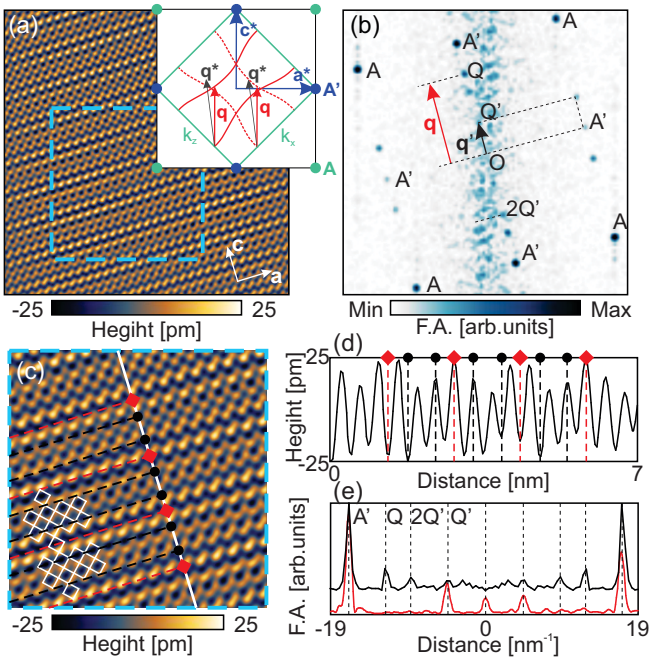

FIG. 2. (Color online) (a) Flittered STM topography obtained for $V_b = 0.2\,\mathrm{V}$ and $I_s = 0.6\,\mathrm{nA}$. The inset shows a sketch of the Fermi surface within the first Brillouin zone (green square whose nodes are A′ points) corresponding to an isolated Te sheet. The dashed (red) lines correspond to the p_x portion of the Fermi surface, whilst the solid (red) lines correspond to the p_z portion of the Fermi surface. The $\mathbf{q}^*$ connects one set of p_x bands. The $\mathbf{q}$ connects both the sets of p_x bands and p_z bands, and is parallel to $\mathbf{c}^*$ vector; (b) The corresponding Fourier transform. A and A′ peaks in the Fourier image correspond to the A and A′ peaks in the inset; (c) Magnified part of image in (a) showing the CDW modulation; (d) Profile along the white line in panel (c); (e) Profile along the main and side diagonals of the Fourier image in panel (b). F.A. stands for Fourier Amplitude.

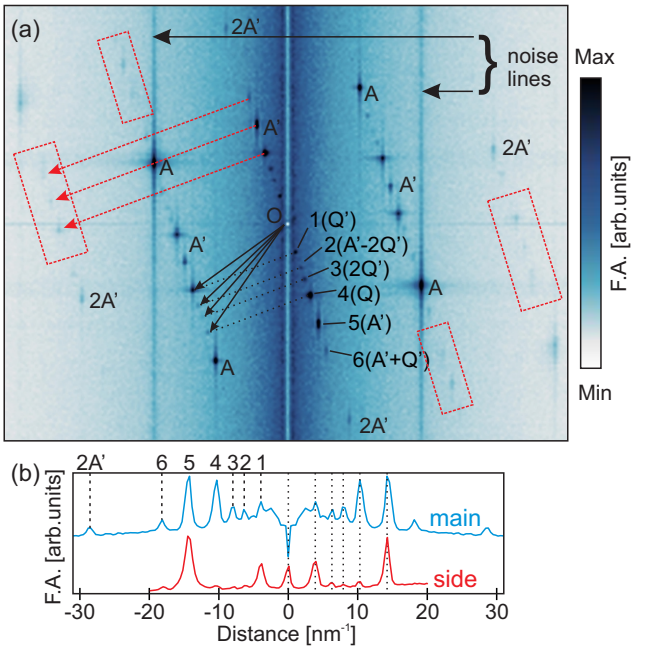

FIG. 3. (Color online) (a) Averaged Fourier transform obtained by summing 34 Fourier transforms which are similar to the one shown in Fig. 1 (b); (b) Profile along the main and side diagonals. Red rectangles mark the areas within which are the Fourier peaks representing copies of the lattice and modulation peaks in higher Brillouin zones. F.A. stands for Fourier Amplitude.

main and side diagonals in order to illustrate that every peak on the main diagonal, except A′+Q′ and 2A′, has its "copy" on the side diagonal.

As noted before, Te sheets are unstable and prone to the CDW. The superspace crystallographic analysis done in Ref. 9 indicated that the distances between neighboring Te atoms in the planar sheets vary around the average of 0.3035 nm in a systematic manner. The total ordering can be viewed as alternate sequences of V and N groups of Te sheet atoms in the direction of the crystallographic c axis (along the CDW modulation). Analyzing Figs. 1 (b) and 1 (c) we have already noted that the interatomic distances between neighboring Te atoms vary around the average of 0.3075 nm, which is slightly higher that the one given in Ref. 9. However, since the distance variations are rather subtle we were not able to confirm the proposed ordering by examining images similar to those in Fig. 1 (b). Therefore, we have chosen the tunneling parameters, $V_b = 0.1\,\mathrm{V}$ and $I_s = 0.7\,\mathrm{nA}$, for which the tip is even closer to the surface than in the case shown in Fig. 2 (a). In this way, the close proximity of a sharp tip to the surface atoms would result in a convolution image such that the atoms being further away from each other would be resolved better than the atoms which are closer to each other (see the sketch in the inset of Figure 4 (a)).

The corresponding topography image is shown in Fig. 4 (a). Next to it (Fig. 4 (b)) is an image formed by measuring the changes of the tunneling current (with respect to I_s) before the feedback moves the piezo scanner in order to maintain the predefined current setpoint. Below them, in Figs. 4 (c) and 4 (d), shown are the corresponding Fourier images.

The topography image in Fig. 4 (a) clearly displays the CDW modulation stripes, as expected, with strange looking shapes in between the stripes. On the other hand, the current image in Fig. 4 (b) displays N and V groups of Te sheet atoms, indicated by higher current values, which have a repeating pattern matching the CDW modulation stripes in Fig. 4 (a). The observed patterns in both topography and current images may originate from the convolution of a damaged (not very sharp) tip and the surface or they may represent a local modification of the surface. That being the case, one would expect to observe new peaks in the Fourier images at the positions defined by wavevectors which are not represented as linear combinations of the lattice and the modulation wavevectors. However, the corresponding Fourier images in Figs. 4 (c) and 4 (d) have almost all of the characteris-

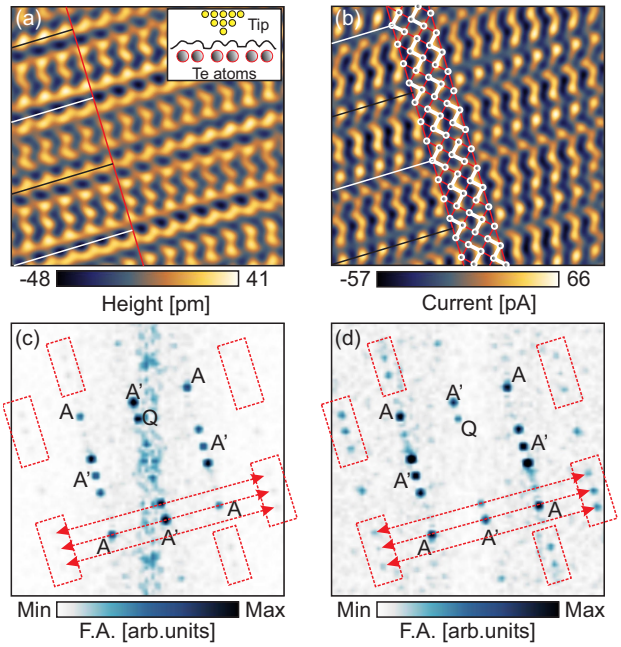

FIG. 4. (Color online) (a) Topography and (b) current images obtained for V_b=0.1 V and I_s=0.7 nA and (c), (d)their corresponding Fourier images. Red rectangles mark the areas within which are the Fourier peaks representing copies of the lattice and modulation peaks in higher Brillouin zones. F.A. stands for Fourier Amplitude.

tic peaks seen in Fig. 2 (b), i.e. A, A′, Q and the copy of Q′ on the side diagonals, without any new features. The absence of the Q′ and 2Q′ peaks from the main diagonals in Figs. 4 (c) and 4 (d) is a consequence of applying Fourier transform to the images scanned over a small area and, of course, a consequence of low signal-to-noise ratio, rather than a consequence of the modification of the carrier density modulation. It is, therefore, natural to assume that only carrier density modulation, lattice features and, as explained, their interplay have an impact on the formation of the image in Figs. 4 (a) and 4 (b), and that the effect of the convolution of the surface with a "bad" tip can be ruled out.

Having in mind that the Fourier images in Figs. 4 (c) and 4 (d) have the same periodic components, one can conjecture that different motifs observed in the topography and current images originate from the different intensities of the Fourier peaks. In fact, the strong CDW stripe motif in the topography image is due to the fact that the Q peaks in Fig. 4 (c) have higher intensity than the A peaks. Oppositely, the current image does not have strong CDW stripe motif because the Q peaks have significantly lower intensity than the rest of the peaks in Fig. 4 (d). On the other hand, the irregular shapes in Fig. 4 (a) and the N and V shapes in Fig. 4 (b) are mainly determined by the intensity of the copies of the Q′ peak on the side diagonals, A and A′ peaks.

The "modulation" features on the side diagonals of the Fourier images may exist due to both carrier density modulation and structural modulation (rearrangement) of the Te sheet atoms. If we were to assume that there is no structural modulation, than the intensity of the aforementioned peaks would be determined by the strength of the tunneling signal from the carrier density modulation components with the corresponding periodicity. If the structural modulation is considered without the carrier density modulation, than the intensity of the related peaks would be determined by the magnitude of the atom displacements. Larger displacements would yield Fourier peaks with high intensity, but would also introduce asymmetry in the intensity of the "modulation" peaks across the side diagonal. Such asymmetry is seen as unequal intensity of the Q′ copies on the side diagonals in Figs. 4 (c) and 4 (d). Similar asymmetry of the intensities of the Q′ copies on the side diagonals can be observed in Fig. 2 (b). The Q′ peak copies in Fig. 2 (b) are, however, weaker in comparison to A and Q peaks, which is why the corresponding topography looks like a square Te lattice to which the carrier density modulation and its components are added. Therefore, the structural modulation seen in Fig. 4 (b) most probably exists also in Figs. 2 (b) and 4 (a) but it is masked by contribution of the other periodic components included in the formation on these images.

Finally, further examination of Fourier images in Figs. 3 (a), 4 (c) and 4 (d) indicates the existence of additional peaks (marked by red rectangles in the mentioned figures) which are located at the positions corresponding to the linear combinations of the lattice and the modulation wavevectors. These peaks are, therefore, copies of the lattice and modulation peaks in higher Brillouin zones, and are expected in systems exhibiting charge density and structural modulations. However, their intensity is very low, especially in Figs. 3 (a) and 4 (c), and comparable to the noise level. Unfortunately, we find that taking larger scans than those shown in Figs. 4 (a) and 4 (b) does not improve signal-to-noise ratio for the additional peaks at room temperature, but rather leads to an unstable operation in which the topography and the current images change their appearance after a certain time of scanning.

B. CDW gap measurement

1. *STS measurements*

The formation of energy gaps is a general characteristic of the CDW systems. In these systems a broken symmetry ground state (CDW state) is stabilized via electron-electron or electron-phonon interactions or both, by creating electron-hole pairs with the ordering vector selected as explained in Section III A. This, in turn, leads to the energy gap formation in the regions of the Fermi surface connected by the preselected ordering vector, thus, lowering the energy of the system. For RTe$_3$ family the Fermi surface is only partially gapped. Here we use STS

in order to assess the CDW gap of $CeTe_3$ at room temperature.

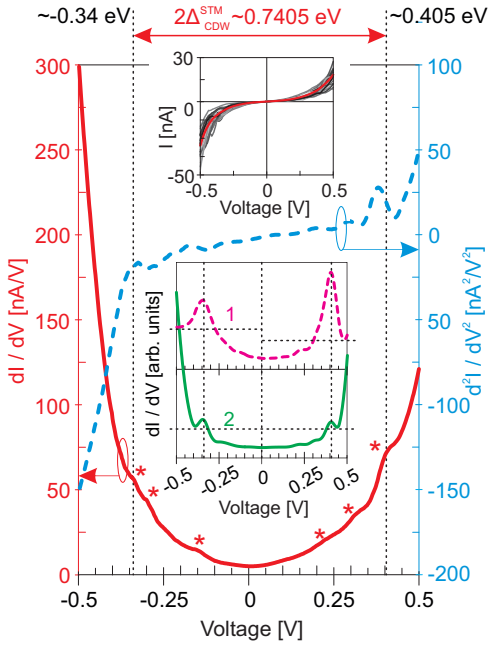

FIG. 5. (Color online) Averaged dI/dV curve obtained by repeated measurements at different positions on the sample and its first derivative. The red asterisks indicate the kinks. The upper inset shows all $I-V$ curves taken into account. The lower inset shows two dI/dV curves obtained by averaging selected dI/dV curves.

Figure 5 shows an averaged dI/dV versus V(red curve) and its first derivative, d^2I/dV^2 (blue curve). In the upper inset shown are the $I-V$ curves collected at different locations on the sample by performing ten consecutive measurements at each location. The averaging procedure was done due to the variation of the $I-V$ curves which are acquired at random points, including ones above and in between the Te sheet atoms. Location dependent variations of the $I-V$ were previously noted in $TbTe_3$.[17] The spatial variation of the $I-V$ curves is consequently reflected on the corresponding dI/dV curves in terms of occasional appearance of different peak-like features and variations of the conductance near the edges of the measuring range.

The asymmetry of the averaged dI/dV curve, is an inherent property of most of the individual dI/dV curves, despite their location dependent variations. It originates from the fact that, apart from the in-plane p_x and p_z orbitals, the p_y orbitals are probed as well.[17] Removal of electrons from p_y, which occurs at negative voltages, is more favorable than the adding of electrons at positive voltages since the p_y orbitals are below the Fermi level. Therefore, the conductance, i.e. dI/dV, will be higher for negative than for positive voltages and, consequently, the dI/dV curves would be asymmetric. This type of dI/dV asymmetry is common among systems exhibiting CDW.[17,18,30–32]

The averaged dI/dV exhibits subtle kinks marked by (red) stars in Fig. 5. For each kink in the dI/dV curve one can observe a change in slope of the corresponding d^2I/dV^2 curve which, indeed, corroborates that the kinks exist. In fact, most of the kinks are a consequence of the location dependent variations of the individual dI/dV curves included in the averaging procedure. They are, therefore, likely due to involvement of the tip states, due some other effect such as zero bias anomaly,[33] or even maybe due to the existence of the shadow gaps in $CeTe_3$.[13] Similar structures can be observed in Ref. 18. Unfortunately, we cannot claim with certainty what they represent nor determine their origin. Exceptions are the two features at $\sim -0.34\,\mathrm{eV}$ and $\sim 0.405\,\mathrm{eV}$, additionally marked by dashed lines, which exist in the most of the measurements. Majority of the individual dI/dV curves exhibit weak features at $\sim -0.34\,\mathrm{eV}$ and $\sim 0.405\,\mathrm{eV}$, whereas a notably smaller number of curves has slightly stronger features at the same energies (the reason why the intensity of these peaks vary is unknown). Hence, the average dI/dV in Fig. 5 also has weak structures at $\sim -0.34\,\mathrm{eV}$ and $\sim 0.405\,\mathrm{eV}$. A sharp rise of the conductance occurring immediately below $\sim -0.34\,\mathrm{eV}$ and above $\sim 0.405\,\mathrm{eV}$ in the average dI/dV indicates that these features may be interpreted as the edges of the CDW gap.[33] However, the density of states within the suggested gap does not appear to be suppressed. This is somewhat expected considering that a large number of curves, having a significant location dependent variation, are averaged. On the other hand, averaging a smaller number of selected curves yields dI/dV spectra with clear features at $\sim -0.34\,\mathrm{eV}$ and $\sim 0.405\,\mathrm{eV}$ and a suppressed density of states between them, as shown in the lower inset of Fig. 5. dI/dV labeled by 1 is obtained by averaging curves with stronger features, whereas dI/dV labeled by 2 is obtained by averaging curves with weaker features at $\sim -0.34\,\mathrm{eV}$ and $\sim 0.405\,\mathrm{eV}$. We, therefore, speculate that the relevant features might be the band edges rising above and below the Fermi level, which correspond to the CDW gap originating from hybridization between the original and shadow bands. We assess the distance between the two features to be $2\Delta_{\mathrm{CDW}} \sim 0.74\,\mathrm{eV}$, yielding a CDW gap of $\sim 0.37\,\mathrm{eV}$. Finally, suppressed density of states, seen in the two curves, along with the fact that both of them have a finite conductance at zero bias suggests a partially gapped Fermi surface, as expected.

2. *Raman scattering measurements*

Polarized Raman spectra of $CeTe_3$ were measured on a cleaved (010) $(a-c)$ plane in the temperature range between 348 and 32 K. Fig. 6 shows the symmetry-resolved spectra for 348 and 32 K which are linear combinations of the raw data. For unknown reasons, the spectra taken at 348 K are generally higher by a factor close to 2 and are therefore multiplied by 0.55 to make them match those at 32 K at high and low energies. The electronic continua

of the multiplied spectra match now also in the range up to 1000 cm^{-1}. Phonons and amplitude modes appear at energies Below 400 cm^{-1}.[34] In addition, there are also features from crystal-field excitations which appear not only in the Raman active A_{1g}, B_{1g} and B_{2g} symmetries but also in A_{2g} symmetry, clearly ruling out a phononic origin. They originate in the energy splitting of the $2F_{7/2}$ state of $CeTe_3$ ($4f$ orbitals) in the spectral region below 400 cm^{-1} and between 2000 and 2500 cm^{-1}.

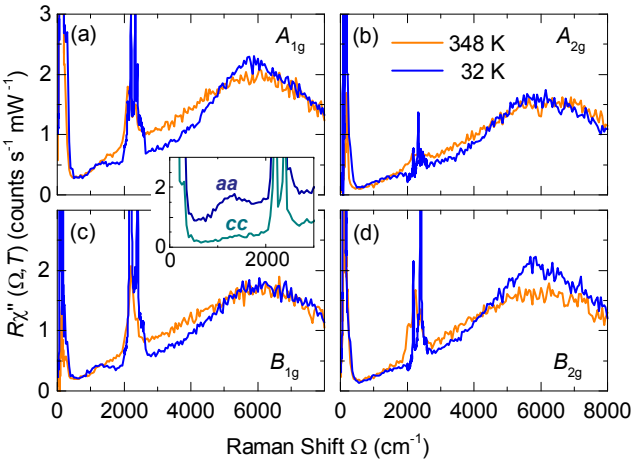

FIG. 6. (Color online) Symmetry-resolved Raman spectra of $CeTe_3$ at temperatures as indicated. The excitations in the range 2000 to 2500 cm^{-1} originate in transitions in the $F_{7/2}$ manifold. They are expected and appear also in A_{2g} symmetry. In all cases there are stronger at low temperature. Gap-like features are predominantly seen in A_{1g}, B_{1g}, and B_{2g} symmetry. The inset in (a) compares the raw data in aa and cc polarization indicating an $a-c$ anisotropy.

Although T_{CDW} is considerably above room temperature (and is not determined yet but believed to be in the 500 to 600 K range) one observes clear changes in the electronic spectra upon cooling. Below 4000-5000 cm^{-1} the opening of a gap manifests itself by a relative reduction of the scattering intensity in the A_{1g}, B_{1g}, and B_{2g} spectra. Around 6000 cm^{-1} the intensity piles up due to emerging coherence effects in the ordered state (Fig. 6 (a), (c), (d)). As expected for electronic excitations these temperature-dependent changes are very weak or absent in A_{2g} symmetry (Fig. 6 (b)). According to the semi-quantitative analysis of the results in $ErTe_3$[12] we interpret the changes described above in terms of an anisotropic CDW gap. The signatures of the gap are weaker than in $ErTe_3$ for two reasons: (i) Even at 348 K $\approx 0.5\,T_{\mathrm{CDW}}$ $CeTe_3$ is already deep in the ordered state, and the gap is almost constant. (ii) $CeTe_3$ has an impurity concentration comparable to that of $LaTe_3$ or $DyTe_3$ well above that of $ErTe_3$, and sharp structures are washed out.[35] Hence the A_{1g}, B_{1g}, and B_{2g} spectra reflect the CDW gap in the electronic excitation spectrum and the maximum at 5880 cm^{-1} = 0.73 eV is close to the maximal gap $2\Delta_{\mathrm{CDW}}$. This energy is excellent agreement with the gap in ARPES experiments[22] and the weak anomalies in the dI/dV curves (see Fig. 5) allowing us to associate them with the gap. Since the gap depends strongly on momentum[22] no pronounced features can be expected in angle integrated experiments such as STS at temperatures on the order of $0.5\,T_{\mathrm{CDW}}$.

Unexpectedly, we observe also an additional maximum in the range 1, 200 cm^{-1} $\sim$ 0.15 eV in A_{1g} and B_{1g} which appears only below approximately 200 K. The appearance in A_{1g} and B_{1g} indicates that the maximum belongs to the lower symmetry of the ordered CDW phase. The comparison of the spectra measured with parallel polarizations along the crystallographic a and c axes (see inset of Fig. 6 (a)) shows that the crystal is mono-domain in the region of the laser spot. The selection rules are exactly those observed before in $ErTe_3$.[12] However there is no indication of a second CDW in other experiments (see, e.g., Ref. 22). In addition, there is no direct correspondence to features in the STS results (see asterisks in Fig. 5) in that the energy observed by light scattering is approximately a factor of two smaller than expected from tunneling. This energy mismatch argues against an relation between the STM feature at -0.15 eV and the Raman peak at the same energy. Speculatively one may associate the second maximum found in the aa-polarized Raman spectra with a hidden transition having a marginally different ordering wave vector and a slightly lower minimum of the free energy as suggested in Refs. 36 and 37. However, the selection rules are more indicative of an ordering wave vector orthogonal to the first one (see gapped cc spectrum *versus* peaked aa spectrum in the inset of Fig. 6 (a)) and argue otherwise. Hence, the maximum at 1, 200 cm^{-1} cannot finally be explained.

IV. SUMMARY

Scanning tunneling microscopy and spectroscopy were used for an investigation of the CDW state in $CeTe_3$. The data was acquired at room temperature. Using Raman spectroscopy we confirmed that $CeTe_3$ is in the CDW state at room temperature. The STM topography images clearly show the presence of the CDW modulation. This fact is supported by spectroscopy curves, which indicate that CDW band gap has a value of $\sim$ 0.37 eV and are in good agrement with gap value of $\sim$ 0.365 eV obtained from Raman measurements. The analysis of the Fourier transform images showed two main peaks along the direction of the CDW. One representing the dominant CDW modulation wavevector, located at $|\mathbf{q}| = 10.26\,\mathrm{nm}^{-1}$, and the other one, $|\mathbf{c}^* - \mathbf{q}| = 4.19\,\mathrm{nm}^{-1}$, interpreted as a consequence of the wavevector mixing effect. The other peaks, which are not related to the Te sheet atoms and Ce subsurface atoms are related both to the mixing effect and possible structural modulations of the Te sheet atoms. The current images indicate periodic patterns of Te sheet atoms grouped in N and V shapes, which were not previously observed by STM.

ACKNOWLEDGEMENT

This work was supported by the Serbian Ministry of Education, Science and Technological Development under Projects ON171032, III45018, OI171005. We acknowledge support by the DAAD through the bilateral project between Serbia and Germany (grant numbers 56267076 and 57142964) and the DFG via the Transregional Collaborative Research Center TRR 80. The collaboration with Stanford University was supported by the Bavarian Californian Technology Center BaCaTeC (grant-no. A5 [2012-2]). Work in the SIMES at Stanford University and SLAC was supported by the U.S. Department of Energy, Office of Basic Energy Sciences, Division of Materials Sciences and Engineering, under Contract No. DE-AC02-76SF00515. Part of the work was carried out at the Brookhaven National Laboratory which is operated by the Office of Basic Energy Sciences, U.S. Department of Energy by Brookhaven Science Associates (DE-SC0012704). We are grateful to Nenad Stojilović for useful discussions.

[1] G. Grüner, *Density Waves in Solids*, edited by D. Pines (Addison-Wesley, Reading, MA, 1994).

[2] G. Ghiringhelli, M. Le Tacon, M. Minola, S. Blanco-Canosa, C. Mazzoli, N. B. Brookes, G. M. De Luca, A. Frano, D. G. Hawthorn, F. He, T. Loew, M. M. Sala, D. C. Peets, M. Salluzzo, E. Schierle, R. Sutarto, G. A. Sawatzky, E. Weschke, B. Keimer, and L. Braicovich, Science **337**, 821 (2012).

[3] Maple, M. B., Hamlin, J. J., Zocco, D. A., Janoschek, M., Baumbach, R. E., White, B. D., Fisher, I. R., and Chu, J.-H., EPJ Web of Conferences **23**, 00012 (2012).

[4] E. DiMasi, M. C. Aronson, J. F. Mansfield, B. Foran, and S. Lee, Phys. Rev. B **52**, 14516 (1995).

[5] H. Yao, J. A. Robertson, E.-A. Kim, and S. A. Kivelson, Phys. Rev. B **74**, 245126 (2006).

[6] N. Ru and I. R. Fisher, Phys. Rev. B **73**, 033101 (2006).

[7] A. Sacchetti, C. L. Condron, S. N. Gvasaliya, F. Pfuner, M. Lavagnini, M. Baldini, M. F. Toney, M. Merlini, M. Hanfland, J. Mesot, J.-H. Chu, I. R. Fisher, P. Postorino, and L. Degiorgi, Phys. Rev. B **79**, 201101 (2009).

[8] A. Sacchetti, E. Arcangeletti, A. Perucchi, L. Baldassarre, P. Postorino, S. Lupi, N. Ru, I. R. Fisher, and L. Degiorgi, Phys. Rev. Lett. **98**, 026401 (2007).

[9] C. D. Malliakas, S. J. L. Billinge, H. J. Kim, and K. M. G., J. Am. Chem. Soc. **127**, 6510 (2005).

[10] C. D. Malliakas and M. G. Kanatzidis, J. Am. Chem. Soc. **128**, 12612 (2006).

[11] N. Ru, C. L. Condron, G. Y. Margulis, K. Y. Shin, J. Laverock, S. B. Dugdale, M. F. Toney, and I. R. Fisher, Phys. Rev. B **77**, 035114 (2008).

[12] H.-M. Eiter, M. Lavagnini, R. Hackl, E. A. Nowadnick, A. F. Kemper, T. P. Devereaux, J.-H. Chu, J. G. Analytis, I. R. Fisher, and L. Degiorgi, Proc. Nat. Acad. Sciences **110**, 64 (2013).

[13] V. Brouet, W. L. Yang, X. J. Zhou, Z. Hussain, N. Ru, K. Y. Shin, I. R. Fisher, and Z. X. Shen, Phys. Rev. Lett. **93**, 126405 (2004).

[14] F. Schmitt, P. S. Kirchmann, U. Bovensiepen, R. G. Moore, L. Rettig, M. Krenz, J.-H. Chu, N. Ru, L. Perfetti, D. H. Lu, M. Wolf, I. R. Fisher, and Z.-X. Shen, Science **321**, 1649 (2008).

[15] R. G. Moore, V. Brouet, R. He, D. H. Lu, N. Ru, J.-H. Chu, I. R. Fisher, and Z.-X. Shen, Phys. Rev. B **81**, 073102 (2010).

[16] R. V. Yusupov, T. Mertelj, J.-H. Chu, I. R. Fisher, and D. Mihailovic, Phys. Rev. Lett. **101**, 246402 (2008).

[17] A. Fang, N. Ru, I. R. Fisher, and A. Kapitulnik, Phys. Rev. Lett. **99**, 046401 (2007).

[18] A. Tomic, Z. Rak, J. P. Veazey, C. D. Malliakas, S. D. Mahanti, M. G. Kanatzidis, and S. H. Tessmer, Phys. Rev. B **79**, 085422 (2009).

[19] W. Tremel and R. Hoffmann, Journal of the American Chemical Society **109**, 124 (1987).

[20] R. Patschke and M. G. Kanatzidis, Phys. Chem. Chem. Phys. **4**, 3266 (2002).

[21] H. J. Kim, C. D. Malliakas, A. T. Tomić, S. H. Tessmer, M. G. Kanatzidis, and S. J. L. Billinge, Phys. Rev. Lett. **96**, 226401 (2006).

[22] V. Brouet, W. L. Yang, X. J. Zhou, Z. Hussain, R. G. Moore, R. He, D. H. Lu, Z. X. Shen, J. Laverock, S. B. Dugdale, N. Ru, and I. R. Fisher, Phys. Rev. B **77**, 235104 (2008).

[23] D. Necas and P. Klapetek, Central European Journal of Physics **10**, 181 (2012).

[24] T. P. Devereaux and R. Hackl, Rev. Mod. Phys. **79**, 175 (2007).

[25] B. Muschler, W. Prestel, L. Tassini, R. Hackl, M. Lambacher, A. Erb, S. Komiya, Y. Ando, D. Peets, W. Hardy, R. Liang, and D. Bonn, Eur. Phys. J. Special Topics **188**, 131 (2010).

[26] B. K. Norling and H. Steinfink, Inorganic Chemistry **5**, 1488 (1966).

[27] A. Kikuchi, J. Phys. Soc. Japan **67**, 1308 (1998).

[28] H.-M. Eiter *et al.*, *Carrier and Lattice Dynamics in Systems with Charge and Spin Order*, Ph.D. thesis, PhD thesis, Technische Universität München (2014).

[29] M. D. Johannes and I. I. Mazin, Phys. Rev. B **77**, 165135 (2008).

[30] T. Machida, Y. Fujisawa, K. Igarashi, A. Kaneko, S. Ooi, T. Mochiku, M. Tachiki, K. Komori, K. Hirata, and H. Sakata, Phys. Rev. B **88**, 245125 (2013).

[31] A. Soumyanarayanan, M. M. Yee, Y. He, J. van Wezel, D. J. Rahn, K. Rossnagel, E. W. Hudson, M. R. Norman, and J. E. Hoffman, Proc. Nat. Acad. Sciences **110**, 1623 (2013).

[32] F. Flicker and J. van Wezel, Nat. Commun. **6**, 1 (2015).

[33] C. Wang, B. Giambattista, C. G. Slough, R. V. Coleman, and M. A. Subramanian, Phys. Rev. B **42**, 8890 (1990).

[34] M. Lavagnini, M. Baldini, A. Sacchetti, D. Di Castro, B. Delley, R. Monnier, J.-H. Chu, N. Ru, I. R. Fisher, P. Postorino, and L. Degiorgi, Phys. Rev. B **78**, 201101 (2008).

[35] T. P. Devereaux, Phys. Rev. B **45**, 12965 (1992).

[36] M. Lavagnini, H.-M. Eiter, L. Tassini, B. Muschler, R. Hackl, R. Monnier, J.-H. Chu, I. R. Fisher, and L. Degiorgi, Phys. Rev. B **81**, 081101 (2010).

[37] W. Hu, Q. Zhang, and N. Wang, Physica C **469**, 545 (2009).